Measurements and Ray Tracing Simulations for Non-Line-of-Sight Millimeter-Wave Channels in a Confined Corridor Environment

GUANGRONG YUE[1], DAIZHONG YU[1], HAO QIU[2], KE GUAN[2], (Senior Member, IEEE), LIN YANG[1], (Member, IEEE), AND QIFU LV[3]

[1]National Key Laboratory of Science and Technology on Communications, University of Electronic Science and Technology of China, Chengdu 611731, China
[2]State Key Laboratory of Rail Traffic Control and Safety, Beijing Engineering Research Center of High-Speed Railway Broadband Mobile Communications, Beijing Jiaotong University, Beijing 100044, China
[3]Glory Wireless Company Ltd., Chengdu 610066, China

Corresponding author: Guangrong Yue (yuegr@uestc.edu.cn)

ABSTRACT This paper presents the radio propagation measurement, simulation, and analytical results in the 41-GHz millimeter-wave band for non-line-of-sight scenarios in a confined in-building corridor environment. High gain directional antennas are used at both the transmitter and receiver to realize long-distance transmission. Directional channel characteristics of the 41-GHz band, including the path loss model, the root-mean-square delay spread, the multipath statistics, the small scale fading characteristics, the power delay profile, and the power levels received from different antenna directions at different locations, are analyzed in detail. Moreover, in the investigation of the path loss models, we employ ray tracing simulations to extend the path loss model to a more general form so that the structural characteristics of the corridor, such as the length of the line-of-sight section and the corridor corner angle, are considered as modeling parameters. The effects of different transmit/receive antenna locations on the path loss model are also investigated. The combined effects of the highly directional antennas and the confined corridor environment on the wireless channel characteristics are analyzed in detail.

INDEX TERMS Millimeter wave measurements, channel models, ray tracing, radio propagation.

I. INTRODUCTION

Due to the increasing demand for high data rate transmission, additional spectrum bands are expected to be exploited to address the spectrum scarcity problem in traditional bands (below 10 GHz) and support more data traffic for various multidata services. Millimeter-wave (mmWave) bands (approximately between 30 GHz and 300 GHz) have abundant unlicensed spectrum bands and can provide GHz-level bands of contiguous spectra, and thus becoming an important candidate to support high-data-rate wireless connection for the next generation of wireless standard [1], [2].

A full understanding of the radio propagation characteristics at mmWave bands for different scenarios plays a vital role for high-efficient system and network design. Due

The associate editor coordinating the review of this manuscript and approving it for publication was Franco Fuschini.

to the high operating frequency, the radio propagation at mmWave bands differs largely from that at traditional bands below 6 GHz. Generally, mmWave frequencies will undergo greater free space attenuation in the first meter of propagation due to the small wavelengths, compared with today's cellular frequencies [3]. Apart from the free space attenuation, atmosphere and rain will also have frequency-dependent attenuation effects on mmWave propagation [4], [5]. Moreover, the propagation characteristics at mmWave bands exhibit large environment-dependence, which emphasizes the requirement for more research on mmWave propagation under different environments.

Most existing studies on mmWave channel measurements have been focused on the 28 GHz, 38 GHz, 60 GHz and 73 GHz bands [6]–[16], A large number of different communication scenarios, such as the base station (BS)-to-mobile station (MS), BS-to-BS, MS-to-MS, and vehicle-to-vehicle

scenarios, have been considered in the work of previous studies [6]–[9]. Measurement campaigns have been conducted in different environments according to various potential applications of mmWave communications, for example, mmWave for indoor short-distance transmissions [10]–[13], for underground mine communications [14], [15], and for high speed train (HST) services [16]–[18].

Given all these studies mentioned above, however, more research on mmWave channel measurements and analysis is required. The main reasons are summarized as follows. Firstly, most existing studies are focused on the mmWave bands such as the 28 GHz and the 60 GHz band. Apart from those 'hot' bands, there are still many other potential mmWave bands that can be further explored. Secondly, note that some environments, such as the urban street-by-street (SBS) environment [19], the tunnel environment [20], [21], and tunnel-like corridor environment, should be taken into account in channel measurements and analysis for better modeling. Moreover, the wireless industry has found the benefit of describing the line-of-sight (LoS) and non-line-of-sight (NLoS) channel characteristics separately. The high directionality and large penetration loss of mmWave propagation highlights the importance of LoS transmission of mmWave. However, the LoS probability in common scenarios, such as urban microcell (UMi) and urban macro cell (UMa) cases, drops exponentially with the 2D transmitter-receiver (TX-RX) separation [4]. The common existence of NLoS scenarios emphasizes the necessity to explore NLoS channel characteristics at mmWave bands specially.

In this work, we present the measurement results that represent the directional channel characteristics in the 41 GHz band (40.5–41.5 GHz) in a NLoS confined tunnel-like corridor. We would like to emphasize the distinguishing features of corridors that differ from most urban microcell (UMi) environments and other indoor environments such as rooms: 1) the power of electromagnetic waves is often coupled within the corridor and prevented from leakage, leading to smaller attenuation but much more reflected multipath components (MPCs) than in other open environments; 2) similar to the street-by-street environments, corridors with multiple turning corners will result in the non-stationarity of path loss (PL) [19]; 3) in corridors, the user equipments (UEs) cannot be assumed to be uniformly distributed within a microcell as in typical UMi environments [22], but along the corridor. Furthermore, to realize long-distance transmission, high-gain narrow-beam antennas are often used in mmWave systems. As revealed by previous studies, narrow-beam antennas will suppress MPCs, resulting in small delay spread (DS) and high Ricean *K* factors [23], [24]. In this paper, the co-impacts of the confined environment and highly directional antennas are investigated. Fundamental data sets representing the channel characteristics in a tunnel-like in-building corridor are acquired from a recent measurement campaign. A parallel Golay correlator is adopted to acquire the complex channel impulse responses (CIRs) for further analysis [25], [26], and a high-performance computing (HPC) cloud-based

ray-tracing (RT) simulator (CloudRT) is utilized to obtain much larger data sets than would be practically feasible to measure [27]. Channel characteristics, including the PL, multipath amplitude statistics, small scale fading statistics, the power delay profile, the root-mean-square (RMS) delay spread, and received power levels from different antenna directions are analyzed in detail.

The channel models, especially the PL model, developed in this paper are suitable for some environments of wireless communications that are composed of crossing routes with turning corners. Some examples of those environments include the indoor corridors, the SBS urban environments, and underground mines. To form the ability of providing reliable mmWave links in those environments, it is necessary to make deep investigations into the mmWave propagation characteristics. Especially, the NLoS mmWave propagation characteristics after the diffraction of turning corners play a pivotal role in the decision on the deployment of BSs and on the selection of core physical-layer technologies, such as the synchronization and equalization strategies. However, at least to the authors' knowledge, few existing works make research on the mmWave propagation characteristics after diffraction and reflection at the 41 GHz band. Besides, the impacts of different antenna locations and different corner angles on mmWave propagation are not modeled. In this paper, these problems are addressed by analyzing the raw data obtained from measurements and RT simulations.

The rest of this paper is organized as follows. We firstly introduce the Golay correlator based channel sounder used to obtain CIRs in Section II. The tunnel-like corridor environment in which the measurement campaign is carried out is presented in Section III. The analysis of the obtained statistics that characterize the NLoS channel in the tunnel-like environment is discussed in Section IV. Finally, we draw a conclusion in Section V.

II. GOLAY CORRELATOR BASED CHANNEL SOUNDER

In the previous studies [11]–[13], propagation measurements in mmWave bands (particularly in the 60 GHz band) are mainly conducted in indoor scenarios with short ranges and a vector network analyzer (VNA) with frequency-sweep method is often used to acquire channel information. In order to characterize the wireless channel for outdoor and long-distance measurements, channel sounders using a sliding correlator at the receiver (RX) are often adopted for measurement campaigns [28]. This paper considers a Golay correlator based channel sounder. Channel impulse responses (CIRs) can be obtained by taking advantage of the special property of the complementary Golay sequences. That is, the sum auto-correlation of two complementary sequences has a unique peak and zero sidelobe, which can be expressed in formula form as

$$R_a(i) + R_b(i) = 2N(i),$$

$$R_a(i) = \sum_{k=-\infty}^{+\infty} a_N(k) a_N(i+k),$$

$$R_b(i) = \sum_{k=-\infty}^{+\infty} a_N(k) a_N(i+k), \qquad (1)$$

where $a_N(k)$ and $b_N(k)$ are the transmitted complementary Golay sequences and $a_N(k) = b_N(k) = 0$ for $k < 0$ and $k > (N-1)$. $\delta(i)$ denotes the Dirac-delta function. After the wireless channel, the received signals are

$$r_a(k) = \sum_{l=-\infty}^{+\infty} a_N(l) h(k-l) + n_a(k),$$

$$r_b(k) = \sum_{l=-\infty}^{+\infty} b_N(l) h(k-l) + n_b(k), \qquad (2)$$

respectively, where $h(k)$ is the CIR and $n_a(k)$ and $n_b(k)$ are zero mean white Gaussian noise with variance σ^2.

Since the received $r_a(k)$ and $r_b(k)$ are correlated with $a_N(k)$ and $b_N(k)$ stored at the receiver respectively, then the CIR can be recovered by summing the correlation results, i.e.,

$$
\begin{aligned}
r_{CIR}(i) &= \sum_{k=-\infty}^{+\infty} a_N(k) r_a(i+k) + \sum_{k=-\infty}^{+\infty} b_N(k) r_b(i+k) \\
&= 2Nh(i) + n_{ab}(i) \qquad (3)
\end{aligned}
$$

where

$$n_{ab}(i) = \sum_{k=-\infty}^{+\infty} a_N(k) n_a(i+k) + \sum_{k=-\infty}^{+\infty} b_N(k) n_b(i+k) \qquad (4)$$

denotes the noise at the output of the Golay correlator. Note that the power of the output noise $n_{ab}(i)$ is $2N\sigma^2$ and the CIR in (3) is magnified by a factor of $2N$. As a result, the signal-to-nosie power ratio (SNR) is magnified by a factor of $2N$. So it is clear that one benefit of the channel sounder using Golay correlator is the magnification of SNR by a factor of $2N$, where N is the length of the complementary Golay sequence. For example, if length-256 complementary Golay sequences are used by the channel sounder, then the SNR will be magnified by approximately 27 dB. The parameters of the channel sounder adopted in this work are listed in TABLE 1. In our measurement campaign, mechanically steerable high gain (24 dBi) horn antennas with half-power beamwidth (HPBW) as narrow as 7° are used at both the TX and RX. The 3D beam pattern for the TX and RX antennas is depicted in Fig. 1.

A benefit of using high gain and highly directive antennas is that the receiver is able to detect the mmWave signals after large attenuations induced by long transmission distance and multiple reflections. Besides, the narrow beamwidth of directional antennas allow us to compare the channel characteristics in different channel directions. Length-256 complementary Golay sequences are mapped to quadrature phase shift keying (QPSK) signals and transmitted at the TX at a rate of 2 Gbps. The sampling frequency of the analog-to-digital converter (ADC) is 4 GHz at the RX. The sampled digital signals are then fed into the Golay correlator on both of the

TABLE 1. Parameters of the mmwave channel sounder at 41-GHz band based on Golay correlator and mechanically steerable horn antennas.

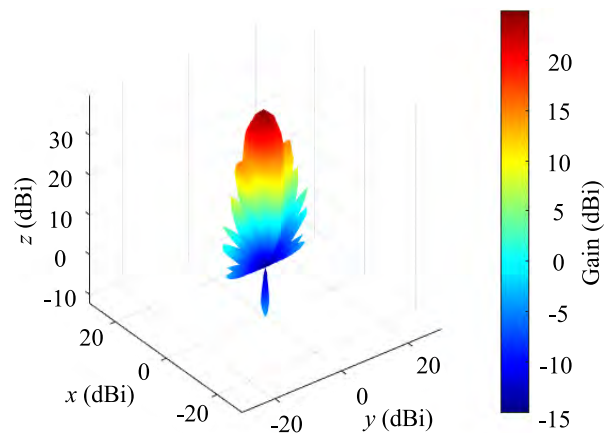|	
Carrier Frequency	41 GHz
Golay Sequence Length	256
RF Bandwidth (Null-toNull)	1.25 GHz
ADC Sampling Frequency	4 GHz
Multipath Time Resolution	0.5 ns
TX & RX Polarization	Vertical
TX & RX Beamwidth (HPBW)	7°
TX & RX Antenna Gain	24 dBi
Receiver gain	54 dB
TX RF Output Power	9.3 dBm
Max. Measurable Path Loss	125 dB
Transmission Tech.	Single Carrier
Modulation Scheme	QPSK

FIGURE 1. The pattern of high gain horn vertically polarized antenna which is modeled by MATLAB.

inphase (I) and quadrature (Q) branches to recover a complex CIR with multipath time resolution of 0.5 ns. Furthermore, it is important to emphasize that both the TX and RX antennas are vertically polarized, and as a result, our measurement results are limited to only the vertical-to-vertical polarized components in a channel.

An example of 1350 PDP snapshots captured in a time window of approximately 1.6 s is shown in Fig. 2, in which the power of each PDP snapshot is normalized to 0 dBw and the time interval between two adjacent PDP snapshots is configured to 0.0012 s. The minimum interval between two adjacent snapshots can be configured to 37.5 μs (0.0012/32 s) to capture the fast fading channel in scenarios such as the train-to-ground communication in high speed train (HST) systems. Due to a lack of time synchronization scheme as mentioned in [29], the captured PDP snapshots are aligned according to their strongest path at reference delay $\tau = 0$ ns, The time synchronization problem can be addressed by either using ray-tracing techniques [29] or by using a function generator that sends trigger signals to both TX and RX and record the propagation delay [30], [31].

In this paper, however, our focus is on the directional channel characteristics in tunnel-like environment and on compar-
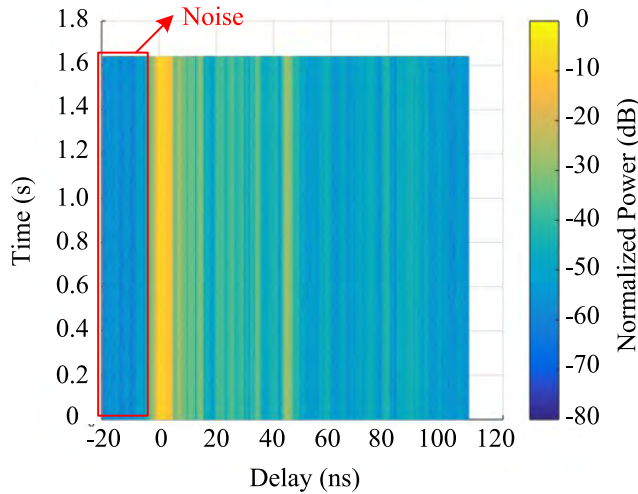
FIGURE 2. An example of 1350 PDP snapshots captured in a time window of 1.62 s, where the power of each PDP snapshot is normalized to 0 dBw and the time interval between two adjacent snapshots is configured to 0.0012 s.
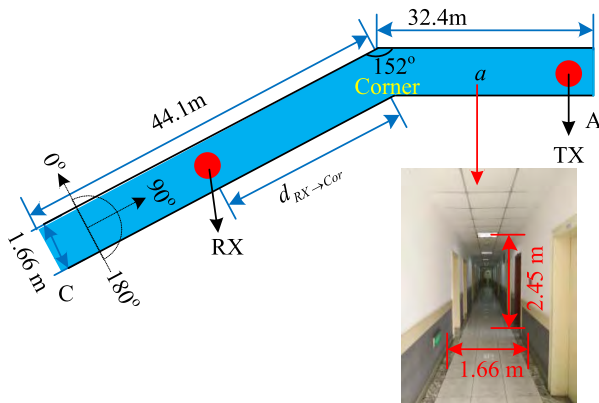

FIGURE 3. Photograph and top view of the corridor where the measurement campaigns were conducted. The corridor consists of two sections (section a and section b) with a sharp corner of 152° between them.

ing the differences of channels at different directions. As a result, the time synchronization scheme is not required in our measurements. The signal at delay interval −20-0 ns in Fig, 2 is the output noise of the Golay correlator and can be used for noise power calculation. In Fig. 2, the maximum recordable delay is 108 ns due to the fact that the Golay sequence length is configured to 256 and the multipath time resolution is 0.5 ns. This maximum recordable delay can be prolonged by simply increasing the length of Golay sequences.

III. MEASUREMENT ENVIRONMENT

The propagation measurements at 41 GHz were conducted in summer of 2018 in a corridor located in the Institute of Fundamental and Frontier Sciences on the Shahe campus of the University of Electronic Science and Technology of China (UESTC), Chengdu, China. There are rooms and laboratories, whose doors are closed during the measurement, along both sides of its main trunk. Besides, as shown in Fig. 3, the corridor is composed of two consecutive sections, denoted

as corridor section *a* and corridor section *b*, whose lengths are 32.4 m and 44.1 m, respectively. There is a sharp corner of 152° between the two corridor sections *a* and *b*. As marked in the photograph in Fig. 3, the width of the corridor is 1.66 m and the height is 2.45 m. The thickness of the concrete walls that separate the main trunk of the corridor and the rooms on both sides is within the range of 25-70 cm.

To measure the TX-Corner and RX-Corner distance accurately, the corridor section *b* and corridor section *a* are discretized into an integral number of steps. As the lengths of corridor sections are 32.4 meters for *a* and 44.1 meters for *b*, the minimum step length unit is chosen as 0.45 meters. As a result, corridor sections *a* and *b* consists of a total number of 72 and 98 step units respectively. As the length of each sliding window to separate small scale fading and large scale fading is selected as 0.4 m to guarantee that no appreciable change (< 5dB) of the average RX power is observed within the span of the window length, the sliding step of the window is chosen as 1.35 meters (3 units) to guarantee successive windows do not overlap. Overall, three forms of measurements are conducted in the corridor:

1) To measure the PL in the corridor, the TX is fixed at the beginning of corridor section *a* (point A) while the RX is driven away from TX at a step of 1.35 m from the starting point that is at the beginning of corridor section *b* (32.4 m away from TX) to the final point that is at the end of corridor section *b*, marked as point B in Fig. 3, A total number of 32 steps are made. The local average power at each step is computed and recorded. In the whole process, both of the TX and RX antennas are steered to the direction of the corridor, pointing to the corridor corner. The receive power values at different TX-RX locations are measured and the overall PL parameters are obtained by finding the minimum mean squared error (MMSE) fitted PL model to the measured data.

2) To obtain the statistic characteristics for the multipath amplitude and small scale fading in the corridor, the RX is driven slowly from the starting point of corridor section *b* towards point C while the TX is fixed at point A. The sliding window method is adopted to remove the effect of large-scale fading [32]. The window length is selected as 40 cm and each window contains a total number of 200 CIR snapshots. In the whole process, the TX-RX heights are configured to 120-120 cm.

3) To compare the received power from different antenna directions, the TX is fixed at point A whereas three locations of the RX in corridor-section *b* are considered: the locations whose distances from the corridor corner are 1.8 m, 16.2 m and 30.6 m, respectively. At each location, the TX antenna is steered to the direction of the corridor while the RX antenna was kept in the horizontal elevation plane and rotated in the azimuth domain from 0° to 180° with sequential increments of 5°, where 90° corresponds to the direction of the corridor. In the process of the measurement, the TX-RX heights are configured to 120-120 cm.

For measurements 1)-3), both of the TX and the RX were placed in the central of the corridor.

IV. MEASUREMENT RESULT

A. PATH LOSS MODEL

The path loss is the inverse of the instantaneous local channel gain. Regardless of the use of directional or omnidirectional antennas, the logarithmic receive power at a 3D distance d from the TX can be written as [1]

$$P_r(d) = P_t + G_t + G_r - PL(d), \quad (5)$$

where G_t and G_r are the TX and RX antenna gains respectively and $PL(d)$ can be modeled as the product of three factors [19]: 1) the inverse of the distance-dependent expected path gain $\overline{PL}(d)$; 2) the zero mean Gaussian distributed random variable representing the shadowing $\mathcal{X}_\sigma$ with standard deviation σ; 3) a random variable representing the small-scale fading that is often averaged out through the use of a sliding window. In other words, the path loss $PL(d)$ in dB can be written as

$$PL(d) = \overline{PL}(d) + \mathcal{X}_\sigma. \quad (6)$$

The distance dependent expected path loss $\overline{PL}(d)$ is commonly modeled as [10], [33]

$$\overline{PL(d)} = PL(d_0) + 10n\log_{10}(d/d_0), \quad (7)$$

where n is the path loss exponent (PLE) and parameter d_0 is the reference distance which can be chosen as the smallest distance for which measurements exist or a fixed value as 1 m. In our measurements, we consider d_0 as 1 m. Parameter d denotes the TX-RX separation, often in terms of 3D Euclidean distance based on the assumption that user equipments (UEs) are uniformly distributed within the cell.

Note that if d is measured in the sense of 3D Euclidean distance, model (7) is consistent with the widely used A-B (or α-β) type model, which can be written as [4]

$$\overline{PL(d)} = \beta + 10\alpha\log_{10}(d/d_0) \quad (8)$$

with $\alpha = n$ and $\beta = PL(d_0)$, and both $PL(d_0)$ (β) and n (α) derived by finding the PL fitting according to the MMSE criterion.

With regard to the communication in corridors, however, the assumption of uniform UE distribution might not be true. Thus, we consider the TX-RX separation d as the length of the path along which the signal reaches RX from TX, as in [10] and [24]. For example, if RX is located at point B and TX is located at point A in Fig. 3, then the TX-RX separation is defined as the length of path A-corner-B.

The PL measurement results are depicted in Fig. 4. In our measurements, we consider four different TX-RX height combinations: 120-120 cm, 120-160 cm, 160-120 cm, and 160-160 cm. For each TX-RX height combination, we find the MMSE-fitted PL model according to (7).

The coefficients of the PL models are listed in TABLE 2, It can be seen that different PL levels are obtained at different

TABLE 2. Path Loss Parameters.

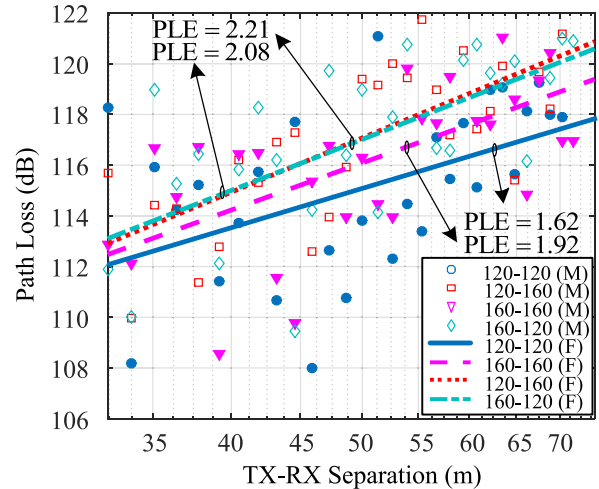| TX-RX Height (cm)	$PL(d)$ (dB)	n	σ (dB)
120-120	87.90	1.62	2.97
160-160	83.47	1.92	2.45
120-160	79.53	2.21	2.15
160-120	81.68	2.08	2.53

FIGURE 4. The measured PL (M) and the best-fitted PL model (F) at different TX-RX antenna heights (cm).

TX-RX height combinations. The PLEs at TX-RX height combinations 120-120 cm, 120-160 cm, 160-120 cm, and 160-160 cm are 1.62, 2.21, 2.08, and 1.92, respectively. The lowest PL level is obtained when both TX and RX antennas are at the height of 120 cm, which is about half of the corridor height (245 m), whereas the highest PL level is obtained at TX-RX heights 120-160 cm and 160-120 cm, when there is a height difference between the TX-RX antennas.

B. PATH LOSS MODEL EXTENDED BY RAY-TRACING SIMULATIONS

1) RT SIMULATION CONFIGURATION

In order to extend the path loss model in the measurements to a more general form, a high-performance computing (HPC) cloud-based ray-tracing (RT) simulator (CloudRT) is utilized in this study. The CloudRT is an open access platform (http://www.raytracer.cloud/). A detailed tutorial of using it can be found in [27].

As shown in Fig. 5, the 3D model of the in-building corridor is reconstructed, where the significant objects: floor, walls, and ceiling are included, with the actual sizes (length of section a: 32.4 m, length of section b: 44.1 m, width: 1.66 m, height: 2.45 m). Both the TX and RX antennas are high gain horn vertically polarized antennas. The pattern of the antenna is shown in Fig. 1. Ray-tracing simulations are conducted at the center frequency of 41 GHz with 1 GHz bandwidth. The key parameters are provided by TABLE 3, where "UTD" stands for the uniform theory of diffraction.
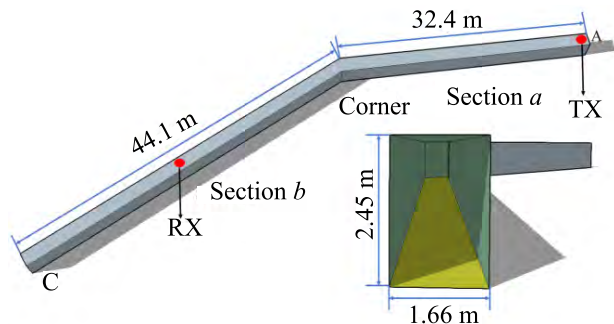
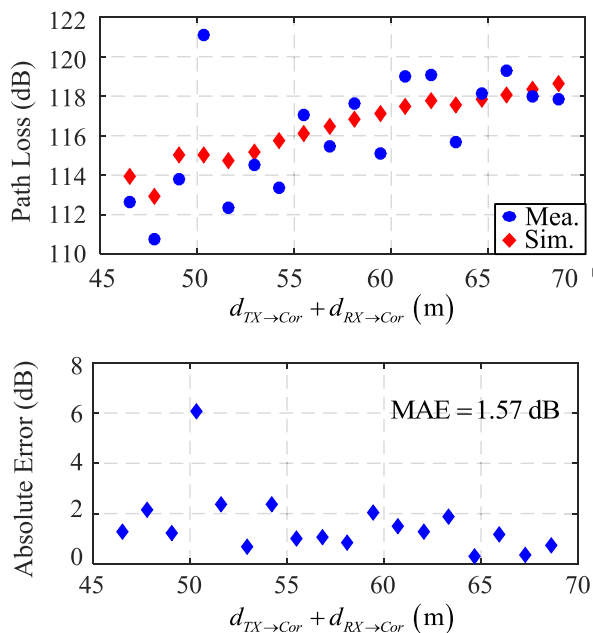**FIGURE 5.** The 3D in-building corridor model reconstructed by SketchUp.

FIGURE 6. The measured PL (Mea.) and the simulated PL (Sim.) at the TX-RX antenna heights of 120-120 cm and the absolute error between measurement and simulation.

TABLE 3. Simulation configuration for ray tracing validation.

Frequency	40.5-41.5 GHz	
Bandwidth	1 GHz	
Antenna	High Gain Horn Antennas	
Propagation Mechanism	Direct	√
	Reflection	Up to 8th Order
	Diffraction	UTD
	Scattering	Directive Scattering Model
	Transmission	×
Material	Wall & Ceiling	Plaster
	Floor	Granite

The comparison of PL between simulation and measurement in the TX-RX antenna height combination of 120-120 cm is shown in Fig. 6, and the good agreement between measurement and simulation can be found. The point-by-point error statics between measurement and

simulation are also shown in Fig. 6, where the mean absolute error (MAE) between measurement and simulation is 1.57 dB. Although at some point, e.g., the point near $d_{TX \to Cor} + d_{RX \to Cor} = 50$ m, relatively large measurement-simulation mismatch is discovered, considering the existence of misalignment and measurement error, this measurement-simulation agreement is sufficient to validate the ray-tracing simulator and the geometric precision of the reconstructed 3D in-building corridor model. Thus, extensive ray-tracing simulations are conducted in order to make further analysis that might not be able to accomplish through merely measurements.

2) THE EXTENDED SBS PL MODEL

In Section IV-A, we model the measured PL with (7), which is also widely used in existing researches [10], [33]. Although Fig. 4 reveals that (7) applies well in the modelling of the measured PL in the corridor environment, (7) does not reflect the characteristics of the corridor, especially in the case when the length of corridor section *a* (denoted by $d_{TX \to Cor}$) and the corner angle at the NLoS transition area change. Thus, we propose applying the street-by-street (SBS) model proposed in [19] to better characterize the PL in corridors, and write the PL model as

$$PL_{NLoS} = 10n_2 \log_{10}\left(\frac{d_{RX \to Cor} + d_{TX \to Cor}}{d_{TX \to Cor}}\right) + PL\left(d_{TX \to Cor}\right) + \mathcal{X}_\sigma, \quad (9)$$

where n_2 denotes the PLE in the NLoS section, and $d_{TX \to Cor}$ and $d_{RX \to Cor}$ denote the length of the LoS section and that of the NLoS section, respectively.

$$PL\left(d_{TX \to Cor}\right) = FSPL\left(f_c, 1\ m\right) + 10n_1 \log_{10}\left(d_{TX \to Cor}\right) + \Delta_{Cor} \quad (10)$$

is the PL at the beginning of the NLoS section, and is formulated according to the close-in free space reference distance path loss (CI) model [4], where $FSPL\left(f_c, 1\ m\right)$, n_1, and Δ_{Cor} denote the free space path loss (FSPL) for frequency f_c at the 1 meter distance, the LoS PLE, and the additional loss induced by the corner respectively. $FSPL\left(f_c, 1\ m\right)$ can be calculated as

$$FSPL\left(f_c, 1\ m\right) = 20 \log_{10}\left(\frac{4\pi f_c \times 10^9}{c}\right)$$
$$= 32.4 + 20 \log_{10}\left(f_c\right). \quad (11)$$

In our system, the carrier frequency is $f_c = 41$ GHz. As a result, the FSPL equals 64.66 dB. $\mathcal{X}_\sigma$ denotes the shadowing with standard deviation σ.

During the measurements and simulations, the length of the LoS section (corridor section *a*) is changed from 18 meters to 32.4 meters at the step of 1.8 meters (4 distance units). For each step, RX is driven along the NLoS section (corridor section *b*) from the corridor corner to the end of the NLoS section at the step of 1.35 meters (3 distance units). At each of those steps, the PL data are recorded for further analysis.
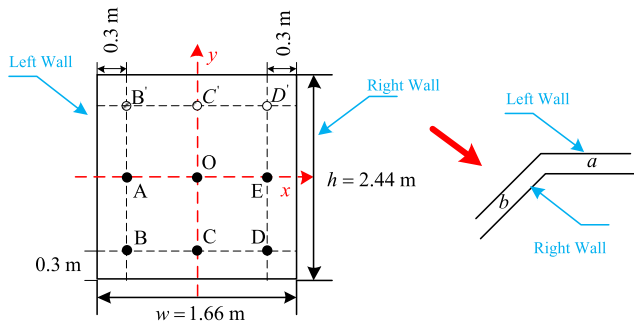
FIGURE 7. The cross section of the corridor and TX and RX antenna locations.

$n_1 = 1.87, n_2 = 2.08, \Delta_{Cor} = 17.09$

FIGURE 8. The 3D PL in the corridor as $d_{TX \to Cor}$ and $d_{RX \to Cor}$ change at the corner angle of $\theta_{Cor} = 152°$.

Apart from $d_{TX \to Cor}$ and $d_{RX \to Cor}$, the locations of TX and RX antennas in the cross-section of the corridor might also have considerable impact on propagation characteristics of mmWave. Fig. 7 depicts the cross-section of the corridor and the nine different locations of TX and RX antennas considered in the measurements and simulations.

1) Point O: the height of point O is 1.22 meters and the distance between O and the left wall is equal to that between O and the right wall, i.e., O is the central point in the cross-section.
2) Point A and E: the heights of A and E are also 1.22 meters, and they are symmetrical about center O with 0.3 meters of antenna-wall distance.
3) Point C: the height of point C is 0.3 meters and the distance between O and the left wall is equal to that between O and the right wall, which is 0.83 meters.
4) Point B and D: the heights of B and D are also 0.3 meters, and they are symmetrical about C with 0.3 meters of antenna-wall distance.
5) Point B', C', and D': B, C, D and B', C', D' are symmetrical about the horizontal axial plane that crosses O, as shown in Fig. 7.

At the corner angle of $\theta_{Cor} = 152°$, channel measurements are conducted at points O, A, B, C, D and E. Since the height of B', C', and D' is above the maximum achievable height in our channel measurement, the PL at B', C', and D' are investigated through RT simulation. At other corner angle values, the raw data are obtained mainly from RT simulation. Hence, the overall PL is derived by integrating the measurement and simulation results and combining the raw data obtained at all TX-RX locations. Based on the fundamental data, important parameters for model (9) can be derived. The derivations for the PL parameters n_2, n_1, and Δ_{Cor} are provided in the Appendix.

Fig. 8 depicts the 3D PL in the corridor as $d_{TX \to Cor}$ and $d_{RX \to Cor}$ change at the corner angle of $\theta_{Cor} = 152°$, where

$$\gamma = \frac{d_{TX \to Cor} + d_{RX \to Cor}}{d_{TX \to Cor}} \quad (12)$$

and the black dots represents the raw data obtained from measurements and simulations. The parameters $n_1 = 1.87$,

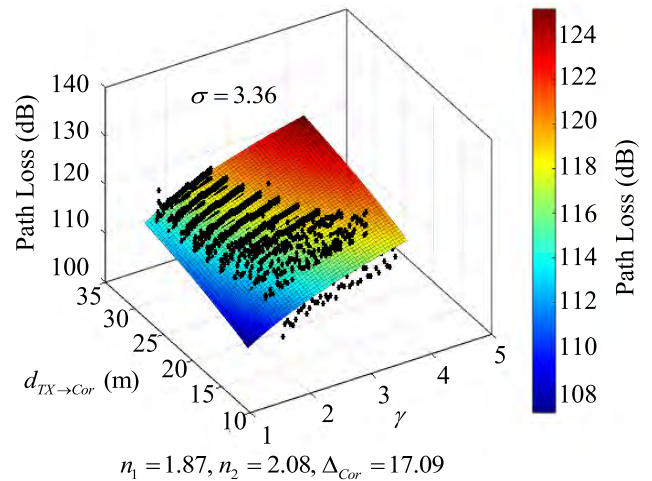$n_2 = 2.08$ and $\Delta_{Cor} = 17.09$ are derived with the MMSE method discussed in the Appendix, and the standard deviation between the raw data and the PL model is $\sigma = 3.36$ dB.

In order to extend the path loss model to a more general form in which the corner angle at the transition corner changes, we update the SBS model (10) to one where the key parameters n_1, n_2, and Δ_{Cor} are functions of the angle of the corridor corner, denoted as θ_{Cor}. To make a distinction between the SBS model extended in this paper and the SBS model proposed in [19], we define the novel model as the extended SBS (ESBS) model. For the simplicity of modeling and application, the linear modeling approach is adopted, i.e., n_1, n_2, and Δ_{Cor} are all viewed as linear functions of θ_{Cor}, and are written as

$$\begin{cases} n_1 = a_{n_1}\theta_{Cor} + b_{n_1} \\ n_2 = a_{n_2}\theta_{Cor} + b_{n_2} \\ \Delta_{Cor} = a_\Delta\theta_{Cor} + b_\Delta. \end{cases} \quad (13)$$

where a_{n_1}, b_{n_1}, a_{n_2}, b_{n_2}, a_Δ and b_Δ are fitting parameters whose values are to be determined through RT simulations. In the simulations, nine different corridor models are reconstructed with corner angles ranging from 90° to 170° with sequential increments of 10°. Fig. (9) depicts the modeling of n_1, n_2, and Δ_{Cor} according to the raw data obtained from RT simulations. It can be observed that n_1, n_2, and Δ_{Cor} decreases as θ_{Cor} becomes larger. However, it can also be seen that the change of n_1 and n_2 due to the change of θ_{Cor} is not obvious, with $a_{n_1} = -0.0030$ and $b_{n_1} = -0.0048$. The decrease of corner loss Δ_{Cor} as θ_{Cor} increases is $a_\Delta = -0.28$ dB per degree. When the corner angle θ_{Cor} changes from 90° to 180°, the difference in corner loss Δ_{Cor} caused by the change of θ_{Cor} reaches 30 dB. It can be also observed that the corner loss approaches 0 dB as θ_{Cor} approaches 180°, this is reasonable considering that the NLoS section (section b) degrades to the LoS section when $\theta_{Cor} = 180°$, and consequently there will be no corner loss in the corridor.
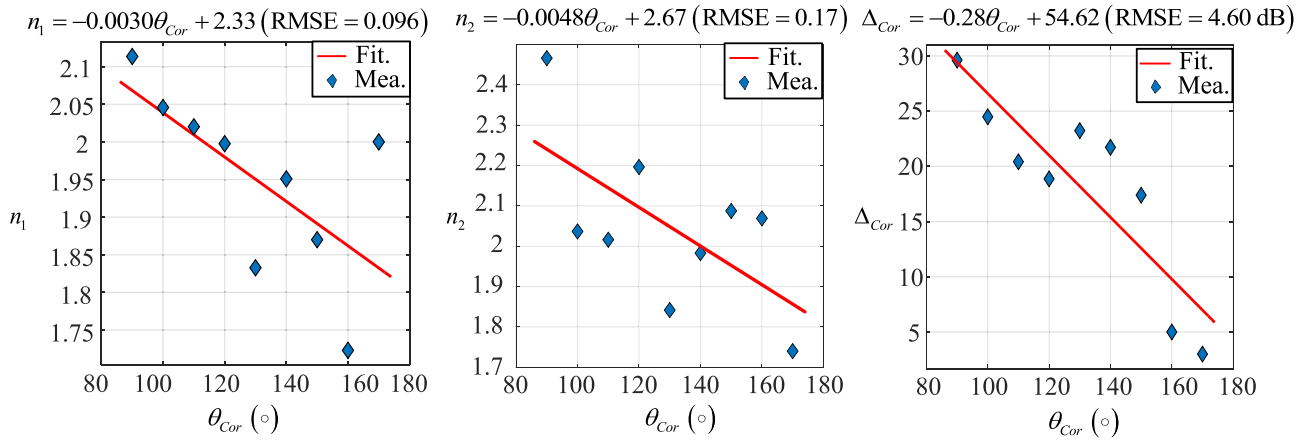
$$n_1 = -0.0030\theta_{Cor} + 2.33 \ (\text{RMSE} = 0.096) \quad n_2 = -0.0048\theta_{Cor} + 2.67 \ (\text{RMSE} = 0.17) \quad \Delta_{Cor} = -0.28\theta_{Cor} + 54.62 \ (\text{RMSE} = 4.60 \ \text{dB})$$

FIGURE 9. The fitting parameters of the extended SBS PL model versus the corner angle θ_{Cor} in the corridor.

Finally, the parameterized PL model can be written as

$$PL_0 (d_{TX \to Cor}, d_{RX \to Cor}, \theta_{Cor})$$
$$= \overline{PL}_0 (d_{TX \to Cor}, d_{RX \to Cor}, \theta_{Cor}) + \mathcal{X}_\sigma, \quad (14)$$

where $\overline{PL}_0 (d_{TX \to Cor}, d_{RX \to Cor}, \theta_{Cor})$, whose expression is given in (15), as shown at the bottom of the next page, denotes the large scale path loss.

As pointed out in [19], conventional PL models are not spatially consistent with the street-by-street urban environment because the corner loss induced by street corners at the intersections of streets is commingled in the shadowing $\mathcal{X}_\sigma$ in conventional models, leading to large rooted mean squared error (RMSE) between the PL model and the raw data. The same is true to some SBS-like environments with one or multiple turning corners, such as the corridor environment investigated in this paper. Thus, the SBS model turns out to be more suitable in those environments than conventional models. Compared with the SBS model, the ESBS model proposed in this paper further considers the corner angle θ_{Cor} as a modeling parameter. More specifically, the SBS model can be viewed as a special case of the ESBS model where the modeling parameters n_1, n_2, and Δ_{Cor} are constants rather than functions of θ_{Cor}.

Note that the modeling parameters might change when the heights of TX/RX antennas change. Moreover, the parameters might be also related to the antenna-sidewall distance. More specifically, the path loss is a function of the antenna locations on the cross section depicted in Fig. 7, denoted as $p_{TX/RX} = (x, y)$. Thus, the PL for a certain TX/RX antenna locations can be written as

$$PL_{NLoS} (d_{TX \to Cor}, d_{RX \to Cor}, \theta_{Cor}, p_{TX}, p_{RX})$$
$$= \overline{PL}_{NLoS} (d_{TX \to Cor}, d_{RX \to Cor}, \theta_{Cor}, p_{TX}, p_{RX}) + \mathcal{X}_\sigma'. \quad (16)$$

where $\overline{PL}_{NLoS}$ denotes the large scale path loss.

Considering that in practical applications, it is more preferable to model the locations of UEs and BSs with random
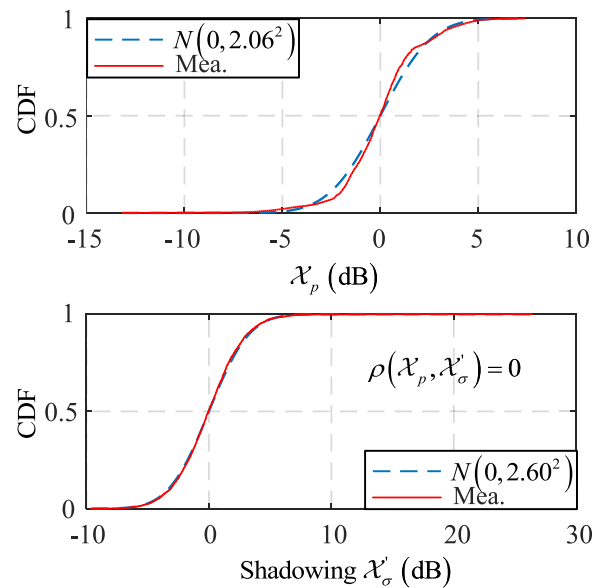

FIGURE 10. The cumulative distribution function of $\mathcal{X}_p$ and $\mathcal{X}'_\sigma$.

variables. We propose modeling the effect of p_{TX} and p_{RX} on PL_{NLoS} with a random variable as well. For a specific pair $\langle p_{TX}, p_{RX} \rangle$, the path loss can be written as

$$PL_{NLoS} (d_{TX \to Cor}, d_{RX \to Cor}, \theta_{Cor}, p_{TX}, p_{RX})$$
$$= \overline{PL}_0 (d_{TX \to Cor}, d_{RX \to Cor}, \theta_{Cor}) + \mathcal{X}_p + \mathcal{X}'_\sigma \quad (17)$$

where $\overline{PL}_0$ is the large scale PL given in (15), which is obtained by combining the measurement and simulation data from all TX/RX antenna locations. $\mathcal{X}_p$ is the difference between $\overline{PL}_{NLoS}$ and $\overline{PL}_0$, i.e., the difference of path loss induced by a specific TX/RX antenna location $\langle p_{TX}, p_{RX} \rangle$. The distribution of $\mathcal{X}_p$ can be found by finding $\overline{PL}_{NLoS}$ through all pairs of $\langle p_{TX}, p_{RX} \rangle$ involved in the measurements and simulations, and find $\mathcal{X}_p = \overline{PL}_{NLoS} - \overline{PL}_0$. The CDFs of $\mathcal{X}_p$ and $\mathcal{X}'_\sigma$ are depicted in Fig. 10, from which it can be

seen that $\mathcal{X}_p$ and $\mathcal{X}'_\sigma$ can be modeled by normal distributions $N\left(0, 2.06^2\right)$ and $N\left(0, 2.60^2\right)$, respectively. Besides, through the calculation of the cross correlation between $\mathcal{X}_p$ and $\mathcal{X}'_\sigma$, denoted as $\rho\left(\mathcal{X}_p, \mathcal{X}'_\sigma\right)$, it can be seen that $\mathcal{X}_p$ and $\mathcal{X}'_\sigma$ are mutually independent variables with $\rho\left(\mathcal{X}_p, \mathcal{X}'_\sigma\right) = 0$, meaning that the PL difference induced by antenna locations is independent of the shadowing. Finally, by modeling the PL variations caused by the variation of p_{TX} and p_{RX} with a random variable $\mathcal{X}_p$, the antenna-location-independent NLoS PL model can be developed as

$$PL_{NLoS}\left(d_{TX \to Cor}, d_{RX \to Cor}, \theta_{Cor}\right)$$
$$= \overline{PL}_0\left(d_{TX \to Cor}, d_{RX \to Cor}, \theta_{Cor}\right) + \mathcal{X}_p + \mathcal{X}'_\sigma \quad (18)$$

with $\overline{PL}_0$ given in (15).

Note that model (18) is consistent with (14) except that the shadowing in $\mathcal{X}_\sigma$ is decomposed into $\mathcal{X}_p$ and $\mathcal{X}'_\sigma$ in (18), i.e.,

$$\mathcal{X}_\sigma = \mathcal{X}_p + \mathcal{X}'_\sigma, \quad (19)$$

where $\mathcal{X}_p$ is related to the TX/RX locations on the cross-section of the corridor, whereas $\mathcal{X}'_\sigma$ is independent of the TX/RX antenna locations.

C. MULTIPATH AMPLITUDES DISTRIBUTIONS

For a wideband transmission system, the complex low pass impulse response of a wireless channel can be modeled by

$$h(t, \tau) = \sum_{n=0}^{N} \alpha_n e^{j\phi_n(t)} \delta\left(\tau - \tau_n\right), \quad (20)$$

where N is the number of multiple paths, and α_n, ϕ_n, τ_n denote the amplitude, phase and arrival time of the n-th path respectively.

In order to obtain the statistical characteristics of the multipath amplitude α_n, we adopt the sliding window method [32] to remove the effect of large-scale path-loss.

To find the proper window length, we adopt the criterion that the running average of RX power should not exhibit appreciable change (< 5 dB) within the span of the window [34] so that wide sense stationarity can be assumed to hold over the span of a window. At first, a sliding-window average of window-length 2 cm (10 successive CIRs) is applied to average out (reduce) the effect of small scale fading so that the running average power at each location can be obtained, i.e.,

$$\bar{P}_i = \frac{1}{10} \sum_{k=0}^{9} P_{i+k}. \quad (21)$$

Then, for each window-length l (m), the average difference between the largest and the smallest received power within a
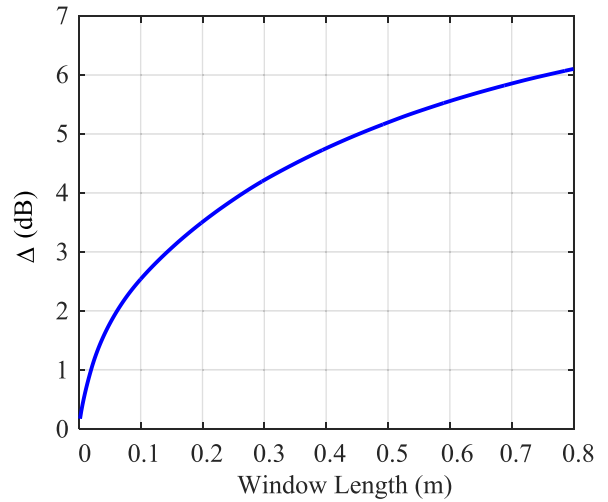

FIGURE 11. Average difference between the largest and the smallest received power within a window in dB vs. window length.

window in dB can be calculated as

$$\Delta(l)\,[dB] = \mathbb{E}_i\left\{\max_{i \le j, k < i+l}\left(\bar{P}_j[dB] - \bar{P}_k[dB]\right)\right\}, \quad (22)$$

where i denotes the index of the beginning CIR snapshot within a window and $\mathbb{E}_i\{\cdot\}$ denotes averaging over all the windows in the corridor where the measurement has been conducted.

Fig. 11 depicts the curve of $\Delta(l)$ as a function of l. We can see that the proper window length should be less than 0.45 m so that the wide sense stationarity will hold. In our measurement, we adopt the window length of 0.4 m which contains 200 CIRs (≈ 55 wavelengths).

In the post processing, we consider three theoretical distribution candidates to model the path amplitude fading: the Rice, the Rayleigh and the lognormal distributions. The Rice and Rayleigh distributions are the most prominent distribution models because they can be justified by the central limit theorem which implies the existence of a large number of statistically independent multipath components (MPCs), whereas the lognormal distribution is justified by the observations in previous studies at traditional bands and explained to be caused by the variation of surrounding obstacles [35]–[37]. The Akaike's information criterion (AIC) is used to select the model that best fits the empirical distribution of the multipath amplitude [38]. The AIC for the j-th candidate distribution is given by

$$AIC_j = -2 \sum_{n=1}^{N} \log_e\left(g_{\hat{\theta}_j}(x_n)\right) + 2U, \quad (23)$$

$$\overline{PL}_0\left(d_{TX \to Cor}, d_{RX \to Cor}, \theta_{Cor}\right) = \left(-0.048\theta_{Cor} + 26.7\right) \log_{10}\left(\frac{d_{RX \to Cor} + d_{TX \to Cor}}{d_{TX \to Cor}}\right)$$
$$+ FSPL\left(f_c, 1\,m\right) + \left(-0.030\theta_{Cor} + 23.3\right) \log_{10}\left(d_{TX \to Cor}\right) + \left(54.62 - 0.28\theta_{Cor}\right); \quad \left(90° \le \theta_{Cor} \le 170°\right), \quad (15)$$
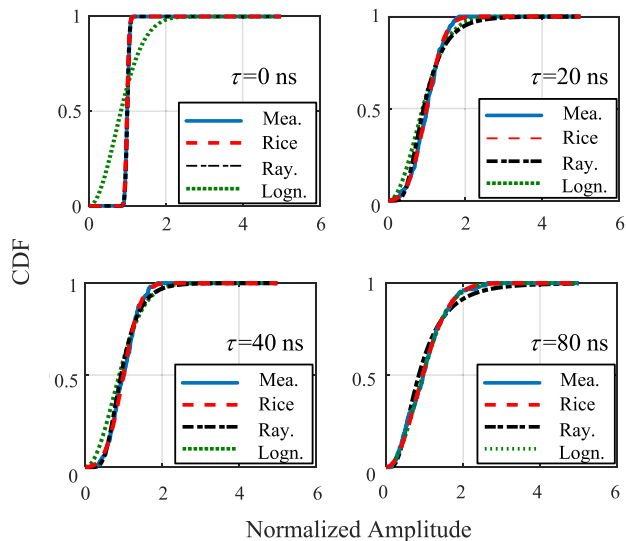
FIGURE 12. Examples of the measured CDFs (Mea.) of multipath amplitudes at excess delays 0 ns, 20 ns, 40ns, and 80 ns in the 1000-th sliding window, and the corresponding best-fitted Rice (Ric.), lognormal (Log.), and Rayleigh (Ray.) CDFs.
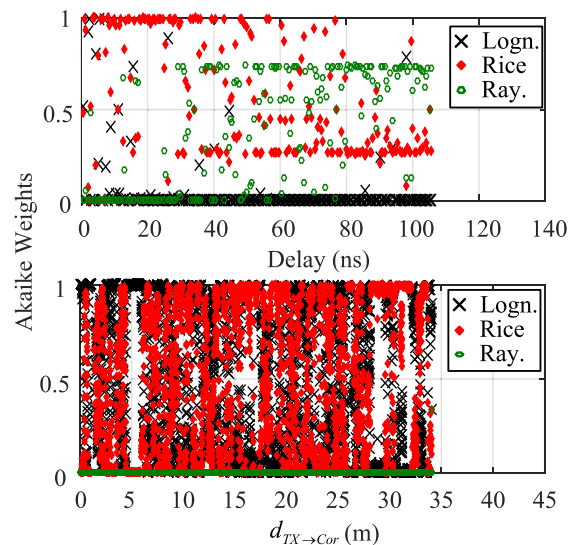

FIGURE 13. Top: Akaike weights for three candidate distributions vs. excess delay based on the measurement results obtained from the 1000-th window; bottom: Akaike weights for three candidate distributions vs. distance based on the measured statistics of the strongest paths.

where $g_{\hat{\theta}_j}(x)$ is the probability density function (PDF) of the candidate distribution, $\hat{\theta}_j$ is the maximum likelihood estimate of the distribution parameter vector θ_j obtained from the measurements, N denotes the size of the sample set and U denotes the dimension of θ_j. To conveniently compare the relative fit of each distribution within the candidate set, we adopt the Akaike weight defined as [39]

$$w_j = \frac{\exp\left(-\left(AIC_j - \min_i AIC_i\right)\Big/2\right)}{\sum\limits_{k=1}^{J} \exp\left(-\left(AIC_k - \min_i AIC_i\right)\Big/2\right)}, \quad (24)$$

where $\sum\limits_{j=1}^{J} w_j = 1$ and the model with the highest Akaike weight can be considered as the best-fitted distribution for the empirical data set. An example of the measured cumulative distribution functions (CDFs) obtained from the 200 CIRs in the 1000-th sliding window and the corresponding best-fitted theoretical Rice, Rayleigh, and lognormal CDFs are depicted in Fig. 12. It can be observed that at excess delay $\tau = 0$ ns, the measured CDF can be well fitted by both of the Rice and the lognormal distribution. Another finding from Fig. 12 is that the empirical multipath amplitude distribution approaches the Rayleigh distribution as the excess delay increases. Fig. 13 shows the Akaike weights for the three candidate distributions vs. excess delays based on the measurements in the 1000-th window (top) and vs. the distance between RX and the corridor corner ($d_{RX \to Cor}$) based on the measured statistics of the strongest path amplitudes from all windows (bottom). We have the following observations: 1) based on the measurements in the 1000-th window, it can be seen that at excess delay ≤ 40 ns, the multipath amplitudes mainly have a Rice distribution, whereas at excess

delay > 40 ns, the Rayleigh weight becomes larger than the Rice weight, implying that the Rice distribution of path amplitudes reduces to Rayleigh distribution as excess delay increases; 2) as for the statistics of the strongest path amplitude, the Rice, the lognormal, and the Rayleigh distribution show the best fit for 54.97%, 45.03%, and 0% of all cases, respectively. Thus, the statistics of the strongest path can be best described by the Rice distribution.

D. SMALL SCALE FADING

For each CIR, the channel transfer function can be obtained by taking the CIR into discrete-time Fourier transform (DTFT), i.e., $H(t, k) = \sum_{n=1}^{N} h(t, n)e^{-\frac{j2\pi kn}{N}}$, where $h(t, n) = a_n e^{j\phi_n}$ is the value of the n-th complex channel tap. We only consider the distribution of $H(t, 1)$, which locates at the center of the bandwidth, for the investigation of small-scale fading statistics. All the obtained coefficients $H(t, 1)$ are normalized with respect to their average power within the window they belong to. The window length is still configured to 40 cm, and the Akaike weight is adopted to find the best model among the Rice, the Rayleigh, and the lognormal distributions in [34], [40].

Fig. 14 (top) gives an example of the empirical CDF and the best-fitted Rice, Rayleigh, and lognormal CDF models based on the measurements (200 CIRs) in the 1000-th sliding window, it can be seen that the empirical CDF can be well fitted by the Rice and the lognormal model. Fig. 14 (bottom) shows the Akaike weights for the Rice, the Rayleigh, and the lognormal distribution model as the window slides at the beginning of corridor section *b* to the point that is 34 m away from the tunnel corner in corridor section *b*. The distance between RX and the corridor corner is denoted as $d_{RX \to Cor}$.

Our results indicate that the Rice, Rayleigh, and lognormal models show the best fit for 69.27%, 2.68%, and 28.05% of
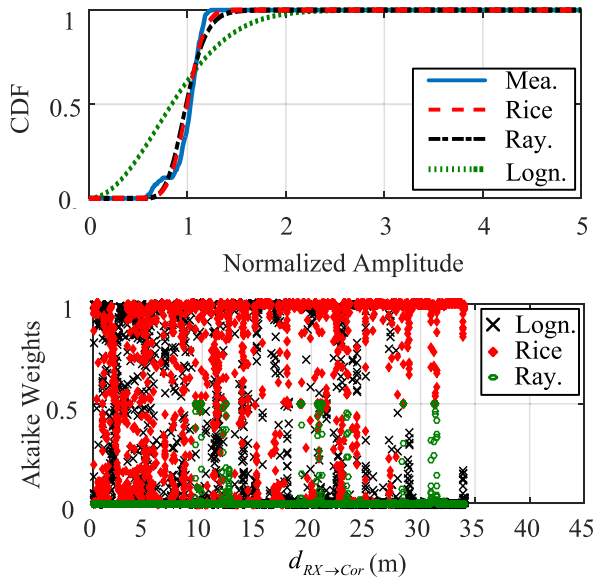
FIGURE 14. Top: An example of the measured CDF (Mea.) in the 1000-th sliding window and the corresponding best fitted Rice (Rice), Rayleigh (Ray.), and lognormal (Logn.) CDF models. Bottom: Akaike weights for three candidate distributions.
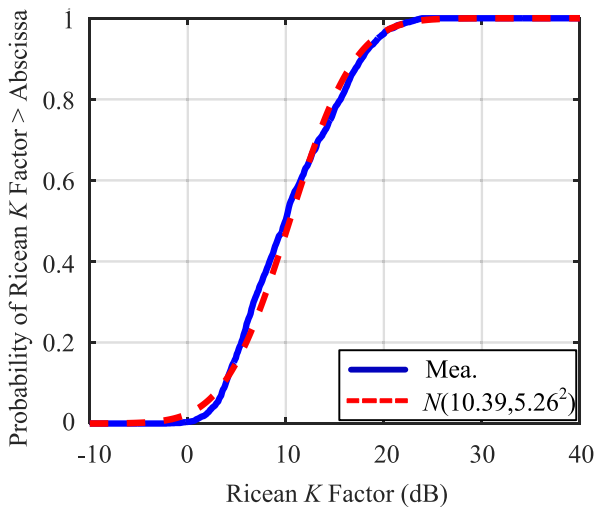

FIGURE 15. CDF of Ricean *K* Factor in the corridor, obtained from the measurements in windows where Rice distribution shows the best fit.

TABLE 4. Rate of the small scale best fit distribution.

Distribution Type	Percentage
Rice	69.27%
Rayleigh	2.68%
lognormal	28.05%

the measurements respectively, as listed in TABLE 4. The predominance of the Rice distribution implies the existence of a steady arriving path and a large number of identically distributed and statistically independent path components. This steady path actually comes along the direction of the corridor, which will be discussed in detail in Section IV-G.

For these cases in which the empirical CDF is best fitted by Rice distribution, the Ricean K factor can be estimated

by [41]

$$\hat{K}_{2,4} = \frac{-2\hat{\mu}_2^2 + \hat{\mu}_4 - \hat{\mu}_2\sqrt{2\hat{\mu}_2^2 - \hat{\mu}_4}}{\hat{\mu}_2^2 - \hat{\mu}_4}. \qquad (25)$$

where $\hat{\mu}_2$ and $\hat{\mu}_4$ are the estimation of the second order moment and the 4-th order moment respectively. The CDF of the Ricean *K* factor obtained from the measurements in windows where Rice distribution shows the best fit is depicted in Fig. 15. It can be observed that the Ricean *K* factor over the corridor is approximately Gaussian distributed and our analysis shows that the empirical distribution can be well fitted by the Gaussian distribution model with mean 10.39 dB and standard deviation 5.26 dB. By comparing the Ricean *K* factor values obtained from our measurements with those from other existing studies, we find that the Ricean *K* factor obtained from our measurement campaign is much larger than that in [34] for indoor scenarios. This is probably because of the fact that TX and RX antennas with approximately omnidirectional azimuth patterns are used in [34], whereas the antennas adopted in this work are highly directive pencil-beam antennas. The measurement results in [10] (Fig. 3) has indicated that the Ricean *K* factor will be significantly increased by using antennas with narrow beams, as a result of the significant suppression of multipath waves when highly directive antennas are used.

E. POWER DELAY PROFILE

The information on the power of the arriving multipath is given in the power-delay profile (PDP), denoted by $|h(t,\tau)|^2$ where $h(t,\tau)$ is given in (20). A very common approximation to the power delay profile is the exponential decay [35], [42]

$$P(\tau) = |h(t,\tau)|^2 \approx A\exp(-B\tau). \qquad (26)$$

To better characterize the PDPs in our measurements, we adopt the 2-section exponential decay model for PDP shape fitting, i.e.,

$$P(\tau) = \begin{cases} 0 & \tau < 0 \\ 1 & \tau = 0 \\ A_1\exp(-B_1\tau) & 0 < \tau < \tau_c \\ P(\tau_c)\exp(-B_2\tau) & \tau > \tau_c \end{cases} \qquad (27)$$

For ready comparison across data sets, $P(\tau)$ is normalized relative to $P(0)$ at first so that $P(0) = 1$ and $B_1, A_1, B_2,$ and τ_c are the PDP shape parameters.

Fig. 16 gives an example of a measured PDP and the corresponding minimum mean squared error (MMSE) curve-fitting according to the shape model provided in (27). It can be seen that the measured PDP corresponds well with the 2-section exponential decay model. The CDFs of the parameters $B_1, A_1, B_2,$ and τ_c obtained from measurements over the corridor are given in Fig. 17, which shows that the CDFs for parameters $B_1, A_1, B_2,$ and τ_c can be well-fitted by CDFs of theoretical lognormal distributions, denoted as $N_{\log}(\mu, \sigma^2)$, where μ and σ are the mean and standard deviation, respectively, of the associated normal distribution.
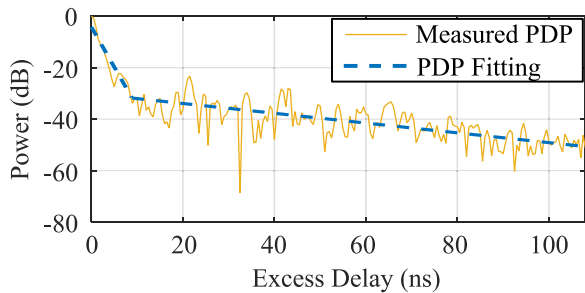
FIGURE 16. Example of the measured PDP and the corresponding curve fitting in dB.
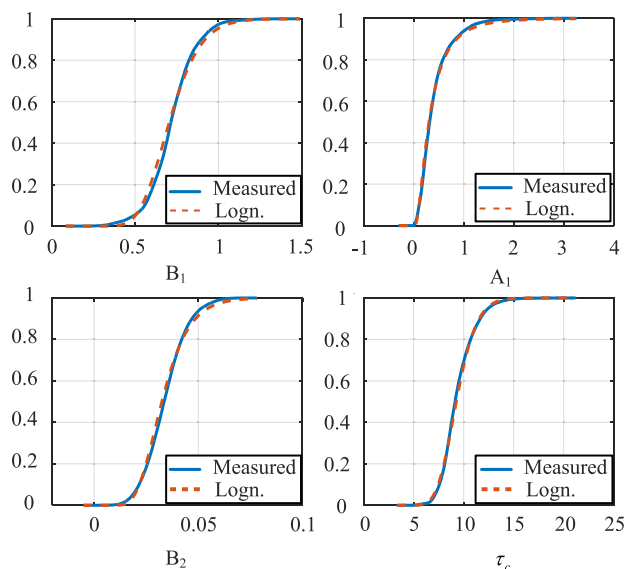

FIGURE 17. Measured CDFs of PDP shape parameters B_1, A_1, B_2, and τ_c and the corresponding best-fitted lognormal CDFs: $N_{\log}\left(-0.35, 0.21^2\right)$, $N_{\log}\left(-1.18., 0.80^2\right)$, $N_{\log}\left(-3.43, 0.31^2\right)$, and $N_{\log}\left(2.23, 0.17^2\right)$ respectively.

The cross correlation coefficient between random variables X and Y, denoted as $\rho(X, Y)$, can be obtained according to the following equation:

$$(X, Y) = \frac{\sum_{n=1}^{N}\left(X_n - \overline{X}\right)\left(Y_n - \overline{Y}\right)}{\sqrt{\sum_{n=1}^{N}\left(X_n - \overline{X}\right)^2 \sum_{n=1}^{N}\left(Y_n - \overline{Y}\right)^2}} \quad (28)$$

Here, X_n and Y_n denote the n-th measured samples for X and Y, and $\overline{X}$ and $\overline{Y}$ denote the sample means of X and Y with the set size of N, respectively. The statistical characteristics of PDP shape parameters B_1, A_1, B_2, and τ_c combined with their pair-wise cross correlation coefficients are listed in TABLE 5, from which we can see that τ_c is highly correlated with B1 and B2 with their cross correlation coefficients greater than 0.5, whereas A_1 can be viewed as independent from B_2 and weakly correlated with (approximately independent from) τ_c.

TABLE 5. Statistical characteristics of the PDP shape parameters.

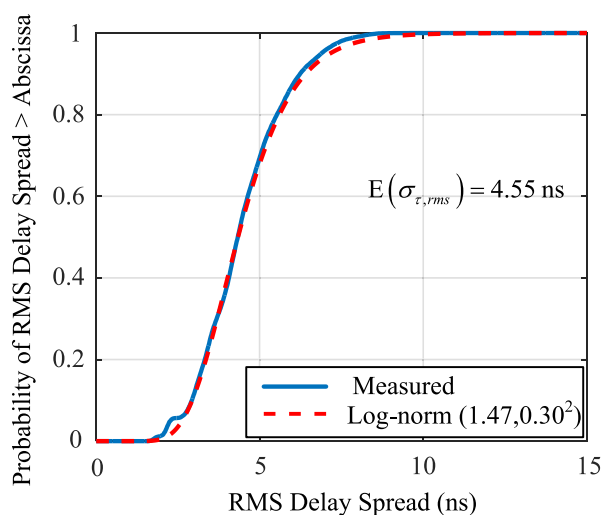| Parameters	Mean	Max	Min	Standard Deviation
	Statistical Characteristics
B_1	0.72	1.40	0.20	0.14
A_1	0.41	3.0	0.01	0.33
B_2	0.034	0.071	0.0019	0.0099
τ_c (ns)	9.4	20	4.9	1.7
	Cross Correlation Coefficients
-	B_1	A_1	B_2	τ_c
B_1	1.00	0.36	0.33	-0.69
A_1	-	1.00	0.00	0.01
B_2	-	-	1.00	-0.65
τ_c	-	-	-	1.00

FIGURE 18. A compare of the overall CDF of measured RMS delay in the corridor and the CDF of lognormal distribution with $\mu = 1.47$ ns and $\sigma = 0.30$ ns.

F. RMS DELAY SPREAD

Root-mean-square (RMS) delay spread is a key factor characterizing the delay dispersion of the wireless channel. With the CIR $h(t, \tau)$ obtained, the RMS delay spread can be calculated as [43]

$$\tau_{rms} = \sqrt{\frac{\sum_k |h(t, \tau_k)|^2 \tau_k^2}{\sum_k |h(t, \tau_k)|^2} - \left(\frac{\sum_k |h(t, \tau_k)|^2 \tau_k}{\sum_k |h(t, \tau_k)|^2}\right)^2}, \quad (29)$$

where τ_k and $|h(t, \tau_k)|$ are the delay and amplitude of the k-th path, respectively.

Fig. 18 shows the empirical CDF of RMS delay spread obtained from 25600 CIRs over the corridor (4 TX-RX heights combinations × 32 locations per combination × 200 CIRs per location). It can be observed that the RMS delay spread values drop in the range of 0 ns and 15 ns with mean 4.55 ns, which is smaller than the NLoS τ_{rms} in rooms and urban environments obtained from the previous studies [6], [10]. The small measured RMS delay spread in our case
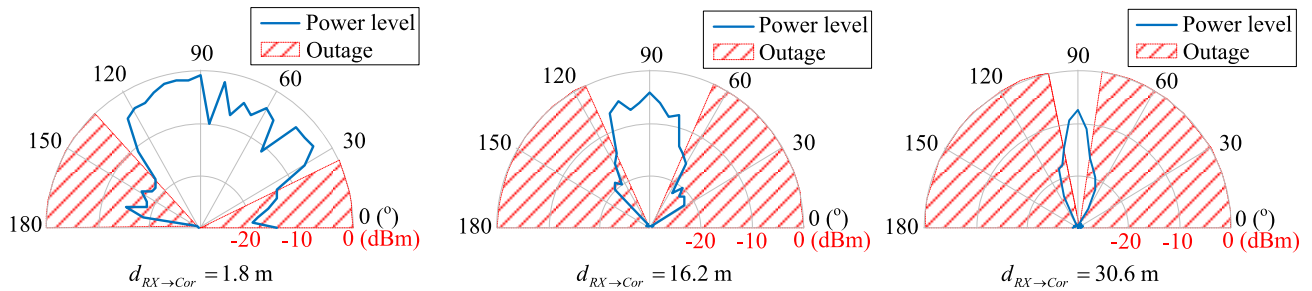
FIGURE 19. A compare of received power (RF output power) level at different directions when the distance between RX and the corridor corner $d_{RX \to Cor} = 1.8$ m, $d_{RX \to Cor} = 16.2$ m, and $d_{RX \to Cor} = 30.6$ m.

might be the result of using high-gain narrow-beam antennas, as the MPCs coming from a wide range of directions would be suppressed by the RX antenna. Another cause to the small RMS delay spread could be the long transmission distance of mmWave in the air. In our case of communication in confined corridors, the mmWave signals are coupled within the confined environment and prevented leakage, which would lead to a large number of MPCs due to the waveguide effect. However, as the TX-RX separation increases, the power of many MPCs will shrink rapidly because of multiple reflections. As a result, when the TX-RX separation becomes sufficiently large, only those MPCs with the least number of reflections (the MPCs propagate along the direction of the corridor) can reach RX, resulting in small RMS delay spread.

G. RECEIVED POWER FROM DIFFERENT DIRECTIONS

To compare the received power from different directions, we utilized a spectrum analyzer (Agilent N9342C) to measure the output power of the radio frequency (RF) front-end. In the mean time, the received RF signal is fed to the Golay channel sounder implemented with field programmable gate arrays (FPGAs) in the based band unit (BBU). In the process, the mmWave TX is located at the starting point of corridor section *a*, as depicted in Fig. 3. Three locations of the RX in corridor section *b* are considered: the locations with $d_{RX \to Cor} = 1.8$ m, $d_{RX \to Cor} = 16.2$ m, and $d_{RX \to Cor} = 30.6$ m, where $d_{RX \to Cor}$ denotes the distance between RX and the corridor corner. Both of the TX and the RX antennas are configured to the height of 120 cm. At each TX-RX location, The TX antenna is pointed to the direction of the corridor section *a*, whereas the RX antenna is kept in the horizontal elevation plane and rotated in the azimuth domain from 0° to 180° in sequential increments of 5°. Here, the azimuth angle 90° in the horizontal elevation plane corresponds to the direction of the corridor, as shown in Fig. 3. Note that an outage could occur at some receive directions, i.e., at those directions, the received power level is below the sensitivity of the digital channel sounder and the CIRs could not be recorded.

Fig. 19 depicts the received power level measured by the spectrum analyzer for the three RX locations considered and marks the directions with a channel sounder outage. It can

be observed that, generally, the received power from each azimuth angle shrinks as $d_{RX \to Cor}$ increases. However, there are still exceptions for this trend. For example, at the azimuth angle of 85°, the receive power is larger in the case of $d_{RX \to Cor} = 16.2$ m than that in the case of $d_{RX \to Cor} = 1.8$ m. If we define the outage rate as the ratio between the range of outage directions with the range of 0° − 180°. It is shown clearly in Fig. 19 that the outage rate increases as $d_{RX \to Cor}$ increases. Let us denote the deviation between the direction of the receive antenna and the direction of the corridor as θ_Δ, i.e.,

$$\theta_\Delta = \left| \theta_{Ant} - 90^o \right|. \qquad (30)$$

where θ_{Ant} denotes the azimuth angle of the receive antenna. It can be seen in Fig. 19 that as $d_{RX \to Cor}$ increases to 16.2 m and 30.6 m, larger receive power is detected at those directions with smaller θ_Δ. For $d_{RX \to Cor} = 1.8$ m (i.e., when the RX is close to the corridor corner), power levels above -10 dBm are observed at directions ranging from 30° to 125°, while this range reduces to 75° − 110° and 85° − 95° for 16.2 m and 30.6 m, respectively, indicating that the signal coming from the direction with large θ_Δ fades faster than the signal from the direction with small θ_Δ. This is reasonable considering that as $d_{RX \to Cor}$ increases, the smaller θ_Δ is, the better the directions of the received rays agree with the direction of the corridor, and the less reflections will those rays experience, resulting in smaller fading caused by reflections. The ray with $\theta_\Delta = 0°$ experiences only one reflection at the corridor corner, becoming the stable path arriving RX, resulting in the Rice distribution of the small-scale fading, as analyzed in Section IV-D.

V. CONCLUSION

This paper presents the measurement results and analysis obtained from a recent measurement campaign conducted in a tunnel-like corridor in UESTC. Our main purpose is to investigate the NLoS channel characteristics, including the PL model, multipath amplitude statistics, small scale fading characteristics, the PDP shape, the RMS delay spread, and the received power level from different antenna directions, when highly directional TX and RX antennas are used.

When analyzing the PL in the NLoS corridor, fundamental data sets are acquired through measurements at first. Then,

based on the validated ray-tracing simulations, the path loss model in the measurements can be extended to a more general form where the characteristics of the corridor structure, including the angle of the corridor corner and the length of the LoS section are considered as modeling parameters. Besides, the impacts of different TX/RX antenna locations on the cross-section of the corridor are modeled through a stochastic approach. The analysis shows that the power loss induced by the corridor corner can be up to 30 dB when the corner angle between LoS and NLoS is 90°, and the corner loss diminishes as the corner angle reaches 180°. The impact of different TX/RX antenna locations can be modeled with a random variable with zero mean and standard deviation 2.06 dB.

The statistical characteristics for the multipath amplitudes and small scale fading are obtained using the sliding-window method. Three theoretical distribution candidates, the Rice Rayleigh and the lognormal distributions, are utilized to model the multipath amplitude and small scale fading. The Akaike information criterion is employed to measure the goodness of fit for the three distribution candidates. Our analysis shows that both the strongest path amplitude and the small scale fading amplitude can be modeled with Rice distribution for most of the cases. The Ricean K factor over the corridor can be modeled by a normal distribution with mean 10.39 dB and standard deviation 5.26 dB.

The empirical PDP shapes over the corridor can be well fitted with the piecewise exponential decay model, whose parameters can be modeled with correlated lognormal variables. The RMS delay spread over the corridor also has a lognormal distribution, with mean 4.55 ns and standard deviation 1.40 ns. The small value of RMS delay might be caused by the highly directional antennas used in the measurement and the long transmission distance.

In the measurement of the received power from different directions, results show that as the TX-RX separation increases, the signal coming along the direction of the corridor fades more slowly than those from other directions do. This is possibly due to the smaller number of reflections experienced by the signal propagated along the direction of the corridor.

APPENDIX A
THE DERIVATION OF SBS PL PARAMETERS
At first, by combining (9) and (10), we obtain

$$PL_{NLoS} = 10n_2\log_{10}\left(\frac{d_{RX\to Cor} + d_{TX\to Cor}}{d_{TX\to Cor}}\right)$$
$$+ FSPL(f_c, 1\,m) + 10n_1\log_{10}(d_{TX\to Cor})$$
$$+ \Delta_{Cor} + \mathcal{X}_\sigma. \quad (31)$$

After substituting $FSPL(f_c, 1\,m)$ with 64.66 dB, which is the FSPL at the 41 GHz frequency, the parameters remain to

be decided are n_1, n_2, and Δ_{Cor}. Let

$$\begin{cases} A = PL_{NLoS}(d_{RX\to Cor}) - FSPL(f_c, 1\,m) \\ B = 10\log_{10}\left(\frac{d_{RX\to Cor} + d_{TX\to Cor}}{d_{TX\to Cor}}\right) \\ C = 10\log_{10}(d_{TX\to Cor}), \end{cases} \quad (32)$$

from which we can obtain

$$\begin{cases} \mathcal{X}_\sigma = A - Bn_2 - Cn_1 - \Delta_{Cor} \\ \sigma = \sqrt{\frac{\sum \mathcal{X}_\sigma^2}{N}} = \sqrt{\frac{\sum(A - Bn_2 - Cn_1 - \Delta_{Cor})^2}{N}} \end{cases} \quad (33)$$

The closed-form solutions for n_1, n_2, and Δ_{Cor} are found by solving for those optimal parameters that minimize the mean squared error (MSE) between the PL model and simulated or measured data. To minimize the mean square error, take the partial derivative of $\sum(A - Bn_2 - Cn_1 - \Delta_{Cor})^2$ with respect to n_1, n_2, and Δ_{Cor} and set the results equal to zero as follows

$$\begin{cases} \frac{\partial \sum(A - Bn_2 - Cn_1 - \Delta_{Cor})^2}{\partial n_2} = 0 \\ \frac{\partial \sum(A - Bn_2 - Cn_1 - \Delta_{Cor})^2}{\partial n_1} = 0 \\ \frac{\partial \sum(A - Bn_2 - Cn_1 - \Delta_{Cor})^2}{\partial \Delta_{Cor}} = 0, \end{cases} \quad (34)$$

from which we can obtain

$$\begin{cases} \sum A - n_2 \sum B - n_1 \sum C - N\Delta_{Cor} = 0 \\ \sum CA - n_2 \sum CB - n_1 \sum C^2 - \Delta_{Cor} \sum C = 0 \\ \sum BA - n_2 \sum B^2 - n_1 \sum BC - \Delta_{Cor} \sum B = 0. \end{cases} \quad (35)$$

where N denotes the total number of samples involved in the calculation, and the parameters n_1, n_2, and Δ_{Cor} can be solved in closed-form by

$$\begin{bmatrix} n_2 \\ n_1 \\ \Delta_{Cor} \end{bmatrix} = \begin{bmatrix} \sum B & \sum C & N \\ \sum CB & \sum C^2 & \sum C \\ \sum B^2 & \sum BC & \sum B \end{bmatrix}^{-1} \begin{bmatrix} \sum A \\ \sum CA \\ \sum BA \end{bmatrix} \quad (36)$$

REFERENCES
[1] T. S. Rappaport, R. W. Heath, Jr., R. C. Daniels, and J. N. Murdock, *Millimeter Wave Wireless Communications*. Englewood-Cliffs, NJ, USA: Prentice-Hall, 2015.
[2] Federal Communications Commission. (Jul. 2016). *Spectrum Frontiers RO and FNPRM: FCC16-89*. [Online]. Available: https://apps.fcc.gov/edocs_public/attachmatch/FCC-16-89A1_Rcd.pdf
[3] T. S. Rappaport, G. R. MacCartney, Jr., M. K. Samimi, and S. Sun, "Wideband millimeter-wave propagation measurements and channel models for future wireless communication system design (invited paper)," *IEEE Trans. Commun.*, vol. 63, no. 9, pp. 3029–3056, Sep. 2015.
[4] T. S. Rappaport, Y. Xing, G. R. MacCartney, A. F. Molisch, E. Mellios, and J. Zhang, "Overview of millimeter wave communications for fifth-generation (5G) wireless networks-with a focus on propagation models," *IEEE Trans. Antennas Propag.*, vol. 65, no. 12, pp. 6213–6230, Dec. 2017.
[5] Z. Qingling and J. Li, "Rain attenuation in millimeter wave ranges," in *Proc. 7th Int. Symp. Antennas, Propag. EM Theory*, Oct. 2006, pp. 1–4.

[6] J. Ko, Y.-J. Cho, S. Hur, T. Kim, J. Park, A. F. Molisch, K. Haneda, M. Peter, D.-J. Park, and D.-H. Cho, "Millimeter-wave channel measurements and analysis for statistical spatial channel model in in-building and urban environments at 28 GHz," *IEEE Trans. Wireless Commun.*, vol. 16, no. 9, pp. 5853–5868, Sep. 2017.

[7] J.-J. Park, J. Lee, K.-W. Kim, K.-C. Lee, and M.-D. Kim, "Vehicle antenna position dependent path loss for millimeter-wave V2V communication," in *Proc. Global Symp. Millim. Waves (GSMM)*, May 2018, pp. 1–3.

[8] V. Petrov, J. Kokkoniemi, D. Moltchanov, J. Lehtomäki, M. Juntti, and Y. Koucheryavy, "The impact of interference from the side lanes on mmWave/THz band V2V communication systems with directional antennas," *IEEE Trans. Veh. Technol.*, vol. 67, no. 6, pp. 5028–5041, Jan. 2018.

[9] G. R. Maccartney, T. S. Rappaport, and A. Ghosh, "Base station diversity propagation measurements at 73 GHz millimeter-wave for 5G coordinated multipoint (CoMP) analysis," in *Proc. IEEE GLOBECOM*, Dec. 2017, pp. 1–7.

[10] H. Yang, P. F. M. Smulders, and M. H. A. J. Herben, "Channel characteristics and transmission performance for various channel configurations at 60 GHz," *EURASIP J. Wireless Commun. Netw.*, vol. 2007, no. 1, pp. 43–47, Jan. 2007.

[11] H. Yang, P. F. M. Smulders, and M. H. A. J. Herben, "Frequency selectivity of 60-GHz LOS and NLOS indoor radio channels," in *Proc. 63rd IEEE Veh. Technol. Conf. (VTC)*, Melbourne, VIC, Australia, vol. 6, May 2006, pp. 2727–2731.

[12] W. Fu, J. Hu, and S. Zhang, "Frequency-domain measurement of 60 GHz indoor channels: A measurement setup, literature data, and analysis," *IEEE Instrum. Meas. Mag.*, vol. 16, no. 2, pp. 34–40, Apr. 2013.

[13] K. Haneda, Jan Järveläinen, A. Karttunen, M. Kyrö, and J. Putkonen, "Indoor short-range radio propagation measurements at 60 and 70 GHz," in *Proc. 8th Eur. Conf. Antennas Propag. (EuCAP)*, Apr. 2014, pp. 634–638.

[14] M. El Khaled, P. Fortier, and M. L. Ammari, "Experimental evaluation of an OFDM millimeter wave system in an underground mine channel based on the IEEE802.15.3c standard," in *Proc. IEEE Int. Conf. Ubiquitous Wireless Broadband (ICUWB)*, Oct. 2015, pp. 1–5.

[15] M. Ghaddar, L. Talbi, M. Nedil, I. B. Mabrouk, T. A. Denidni, "Mm-waves propagation measurements in underground mine using directional MIMO antennas," *IET Microw., Antennas Propag.*, vol. 10, no. 5, pp. 517–524, Apr. 2016.

[16] T. Hattori and T. Kudo, "Propagation experiment on millimeter wave for high-speed rail trains," in *Proc. IEEE 27th Annu. Int. Symp. Pers., Indoor, Mobile Radio Commun. (PIMRC)*, Sep. 2016, pp. 1–6.

[17] G. Li, B. Ai, K. Guan, R. He, Z. Zhong, B. Hui, J. Kim, "Channel characterization for mobile hotspot network in subway tunnels at 30 GHz band," in *Proc. IEEE 83rd Veh. Technol. Conf. (VTC Spring)*, May 2016, pp. 1–5.

[18] G. Noh, J. Kim, Hee S. Chung, B. Hui, Y.-M. Choi, and I. Kim, "mmWave-based mobile backhaul transceiver for high speed train communication systems," in *Proc. IEEE Globecom Workshops (GC Wkshps)*, Dec. 2017, pp. 1–5.

[19] A. F. Molisch et al., "Spatially consistent path loss modeling for millimeter-wave channels in urban environments," in *Proc. Eur. Conf. Antennas Propag. (EuCAP)*, Davos, Switzerland, Apr. 2016, pp. 1–5.

[20] Z. Sun and I. F. Akyildiz, "Channel modeling of wireless networks in tunnels," in *Proc. IEEE Global Telecommun. Conf.*, Nov./Dec. 2008, pp. 1–5.

[21] C. Zhou, "Ray tracing and modal methods for modeling radio propagation in tunnels with rough walls," *IEEE Trans. Antennas Propag.*, vol. 65, no. 5, pp. 2624–2634, May 2017.

[22] *Study 3D Channel Model for LTE (Relaease 12)*, document 3GPP TR 36.873 V12.0.0, Sep. 2014. [Online]. Available: http://www.3gpp.org/ftp/Specs/archive/36_series/36.873/36873-c00.zip

[23] M. Kyrö, S. Ranvier, V.-M. Kolmonen, K. Haneda, and P. Vainikainen, "Long range wideband channel measurements at 81–86 GHz frequency range," in *Proc. 4th Eur. Conf. Antennas Propag.*, Apr. 2010, pp. 1–5.

[24] P. F. M. Smulders, "Statistical characterization of 60-GHz indoor radio channels," *IEEE Trans. Antennas Propag.*, vol. 57, no. 10, pp. 2820–2829, Oct. 2009.

[25] C.-F. Wu, W.-C. Liu, C.-C. Tsui, C.-Y. Liu, M.-S. Sie, and S.-J. J. Jou, "Golay-correlator window-based noise cancellation equalization technique for 60-GHz wireless OFDM/SC receiver," *IEEE Trans. Very Large Scale Integr. (VLSI) Syst.*, vol. 24, no. 11, pp. 3323–3333, Nov. 2016.

[26] B. M. Popovic, "Efficient golay correlator," *Electron. Lett.*, vol. 35, no. 17, pp. 1427–1428, Aug. 1999.

[27] D. He, B. Ai, K. Guan, L. Wang, Z. Zhong, and T. Kürner, "The design and applications of high-performance ray-tracing simulation platform for 5G and beyond wireless communications: A tutorial," *IEEE Commun. Surveys Tuts.*, vol. 21, no. 1, pp. 10–27, 1st Quart., 2019.

[28] R. J. Pirkl and G. D. Durgin, "Optimal sliding correlator channel sounder design," *IEEE Trans. Wireless Commun.*, vol. 7, no. 9, pp. 3488–3497, Sep. 2008.

[29] M. K. Samimi and T. S. Rappaport, "3-D statistical channel model for millimeter-wave outdoor mobile broadband communications," in *Proc. IEEE Int. Conf. Commun. (ICC)*, Jun. 2015, pp. 2430–2436.

[30] S. Hur, Y. Cho, J. Lee, N.-G. Kang, J. Park, and H. Benn, "Synchronous channel sounder using horn antenna and indoor measurements on 28 GHz," in *Proc. IEEE Int. Black Sea Conf. Commun. Netw. (BlackSeaCom)*, May 2014, pp. 83–87.

[31] J. Ko, K. Lee, Y.-J. Cho, S. Oh, S. Hur, N.-G. Kang, J. Park, D.-J. Park, D.-H. Cho, "Feasibility study and spatial–temporal characteristics analysis for 28 GHz outdoor wireless channel modelling," *IET Commun.*, vol. 10, no. 17, pp. 2352–2362, Nov. 2016.

[32] R. He, Z. Zhong, B. Ai, G. Wang, J. Ding, and A. F. Molisch, "Measurements and analysis of propagation channels in high-speed railway viaducts," *IEEE Trans. Wireless Commun.*, vol. 12, no. 2, pp. 794–805, Feb. 2013.

[33] Y. Yu, J. Dong, A.-P. Ye, B. Yang, J. Liu, Y. Liu, W.-J. Lu, and H.-B. Zhu, "Effect of antenna height on propagation characteristics under indoor stair environment," in *Proc. 3rd Asia–Pacific Conf. Antennas Propag.*, Jul. 2014, pp. 710–712.

[34] S. Wyne, A. P. Singh, F. Tufvesson, and A. F. Molisch, "A statistical model for indoor office wireless sensor channels," *IEEE Trans. Wireless Commun.*, vol. 8, no. 8, pp. 4154–4164, Aug. 2009.

[35] M. K. Awad, K. T. Wong, and Z. B. Li, "An integrated overview of the open literature's empirical data on the indoor radiowave channel's delay properties," *IEEE Trans. Antennas Propag.*, vol. 56, no. 5, pp. 1451–1468, May 2008.

[36] L. Dossi, G. Tartara, and F. Tallone, "Statistical analysis of measured impulse response functions of 2.0 GHz indoor radio channels," in *Proc. IEEE Int. Conf. Commun. ICC*, Seattle, WA, USA, Jun. 1995, pp. 1153–1157.

[37] T. Rappaport and C. D. McGillem, "UHF fading in factories," *IEEE J. Sel. Areas Commun.*, vol. 7, no. 1, pp. 40–48, Jan. 1989.

[38] H. Akaike, "Information theory and an extension of the maximum likelihood principle," in *Proc. Int. Symp. Inf. Theory*, Budapest, Hungary, Jan. 1973, pp. 610–624.

[39] U. G. Schuster and H. Bolcskei, "Ultra-wideband channel modeling on the basis of information-theoretic criteria," *IEEE Trans. Wireless Commun.*, vol. 6, no. 7, pp. 2464–2475, Jul. 2007.

[40] S. Lin, L. Kong, L. He, K. Guan, B. Ai, Z. Zhong, and C. Briso-Rodríguez, "Finite-state Markov modeling for high-speed railway fading channels," *IEEE Antennas Wireless Propag. Lett.*, vol. 14, pp. 954–957, 2015.

[41] C. Tepedelenlioglu, A. Abdi, and G. B. Giannakis, "The Ricean K factor: Estimation and performance analysis," *IEEE Trans. Wireless Commun.*, vol. 2, no. 4, pp. 799–810, Jul. 2003.

[42] A. A. M. Saleh and R. Valenzuela, "A statistical model for indoor multipath propagation," *IEEE J. Sel. Areas Commun.*, vol. SAC-5, no. 2, pp. 128–137, Feb. 1987.

[43] A. F. Molisch, *Wireless Communication*. Hoboken, NJ, USA: Wiley, 2007.

GUANGRONG YUE received the Ph.D. degree in communication and information systems from the University of Electronic Science and Technology of China, Chengdu, China, in 2006, where he has been a Faculty Member of telecommunications engineering, since 2008. He was a Postdoctoral Fellow of the Department of Electrical Engineering and Computer Science, University of California at Berkeley, from 2007 to 2008. His major research interests include the wireless communication theory, millimeter wave communications, and adaptive signal processing.

DAIZHONG YU received the B.S. degree from the University of Electronic Science and Technology of China, in 2016, and the master's degree from the National Key Laboratory of Communication, University of Electronic Science and Technology of China, Chengdu, China, in 2016. His current research interests include the fields of the measurement and the modeling of wireless propagation channels, high-speed railway communications, and millimeter-wave communication systems.
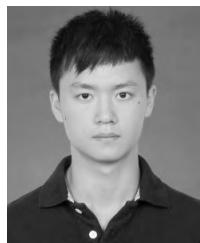
HAO QIU is currently pursuing the master's degree with the State Key Laboratory of Rail Traffic Control and Safety, School of Electronic and Information Engineering, Beijing Jiaotong University, in 2019. His current research interests include the fields of the measurement and the modeling of wireless propagation channels, high-speed railway communications, vehicle-to-x channel characterization, and indoor channel characterization for high-speed short-range systems including future terahertz communication systems.

KE GUAN received the B.E. and Ph.D. degrees from Beijing Jiaotong University, in 2006 and 2014, respectively. He is currently an Associate Professor with the State Key Laboratory of Rail Traffic Control and Safety, School of Electronic and Information Engineering, Beijing Jiaotong University. In 2015, he has received the Humboldt Research Fellowship for Postdoctoral Researchers. He was a recipient of the 2014 International Union of Radio Science (URSI) Young Scientist Award. His papers has received seven best paper awards. In 2009, he was a Visiting Scholar with the Universidad Politecnica de Madrid, Spain, where he was invited to conduct joint research with the Universidad Politecnica de Madrid, from 2013 to 2014. From 2011 to 2013, he has been a Research Scholar with the Institut für Nachrichtentechnik (IfN), Technische Universitaet Braunschweig, Germany. He has received the First National Scholarship for Ph.D. Candidates, in 2012, and the Huawei Excellent Student Award of China, in 2013. He has authored or coauthored two books and one book chapters, and more than 180 journals and conference papers. He held one patent. His current research interests include the fields of measurement and the modeling of wireless propagation channels, high-speed railway communications, vehicle-to-x channel characterization, and indoor channel characterization for high-speed short-range systems, including future terahertz communication systems. He currently serves as a TPC Member of many IEEE conferences such as GLOBECOM, ICC, and VTC. He has been a member of the IC1004 and CA15104 initiatives. He serves as the Publicity Chair of PIMRC, in 2016, the Publicity Co-Chair of ITST, in 2018, the Track Co-Chair of EuCNC, and the Session Convener of EuCAP, in 2015, 2016, 2017, and 2018. He is the Pole Leader of the European Railway Research Network of Excellence (EURNEX). He is an Editor of IEEE Access, the *IET Microwave*, *Antenna and Propagation*, and *Physical Communication*, and a Guest Editor of the IEEE Transactions on Vehicular Technology.

LIN YANG (M'13) received the B.S., M.S., and Ph.D. degrees from Nanjing University. From 2011 and 2012, he was a Research Fellow of the Department of Electronic Engineering, City University of Hong Kong. He is currently an Associate Professor with the National Key Laboratory of Communication, University of Electronic Science and Technology of China, Chengdu, China. His current research interests include multiple-input–multiple-output, orthogonal frequency division multiplexing, non-orthogonal multiple access, and millimeter wave communication systems.
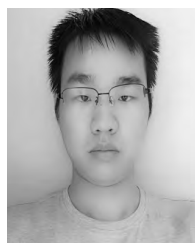
QIFU LV received the bachelor's and master's degrees from Fuzhou University, in 2011, and the University of Electronic Science and Technology of China, in 2014. He joined Chengdu Glory Wireless Company Ltd., in 2016, after three years with Zhuhai Allwinner Technology Company Ltd. His research interests include the fields of millimeter-wave communication and digital circuit design.

• • •